Cell spheroid viscoelasticity is deformation-dependent

Boot, Ruben C.; van der Net, Anouk; Gogou, Christos; Mehta, Pranav; Meijer, Dimphna H.; Koenderink, Gijsje H.; Boukany, Pouyan E.

scientific reports

Check for updates

OPEN

Cell spheroid viscoelasticity is deformation-dependent

Ruben C. Boot[1], Anouk van der Net[2], Christos Gogou[2], Pranav Mehta[1,3], Dimphna H. Meijer[2], Gijsje H. Koenderink[2] & Pouyan E. Boukany[1]✉

Tissue surface tension influences cell sorting and tissue fusion. Earlier mechanical studies suggest that multicellular spheroids actively reinforce their surface tension with applied force. Here we study this open question through high-throughput microfluidic micropipette aspiration measurements on cell spheroids to identify the role of force duration and spheroid deformability. In particular, we aspirate spheroid protrusions of mice fibroblast NIH3T3 and human embryonic HEK293T homogeneous cell spheroids into micron-sized capillaries for different pressures and monitor their viscoelastic creep behavior. We find that larger spheroid deformations lead to faster cellular retraction once the pressure is released, regardless of the applied force. Additionally, less deformable NIH3T3 cell spheroids with an increased expression level of alpha-smooth muscle actin, a cytoskeletal protein upregulating cellular contractility, also demonstrate slower cellular retraction after pressure release for smaller spheroid deformations. Moreover, HEK293T cell spheroids only display cellular retraction at larger pressures with larger spheroid deformations, despite an additional increase in viscosity at these larger pressures. These new insights demonstrate that spheroid viscoelasticity is deformation-dependent and challenge whether surface tension truly reinforces at larger aspiration pressures.

The physical response of multicellular tissues to an applied stress is critical in the regulation of various physiological processes, such as embryonic morphogenesis[1,2], wound healing[3], cell differentiation[4], and cancer metastasis[5,6]. While the mechanical response of single cells is mostly regulated by their cytoskeleton, plasma membrane and nuclear stiffness[7,8], overall tissue mechanics is additionally dependent on intercellular adhesions and the extracellular environment[9–11]. When tissues form and merge, their resulting morphology is defined by this mechanical interplay between cells across multiple length scales, called tissue fluidity[12–14].

To examine the relation between cellular mechanics and tissue fluidity, dissociated cells can be manipulated into a spherical assembly, termed spheroid, by letting them sediment and aggregate in a confined space. Spheroids have become a widely used in vitro model as they recreate both the multicellularity and three-dimensional (3D) microenvironment of in vivo tissues[15,16]. They round up over time, which can be seen as a minimization of surface energy, similar to liquid droplets[17]. Through this analogy, previous studies have defined and experimentally determined a spheroid surface tension γ, which has been related to tissue spreading[18] and cell sorting[19]. Here, the magnitude of γ and the related cellular arrangement depend on the interplay between the intercellular adhesion and cortical tension of the cells[20–22].

A conventional biophysical tool to measure γ is micropipette aspiration (MPA), where a part of the spheroid is aspirated into a micron-sized pipette under a constant stress and the advancing creep length $L(t)$ of the spheroid protrusion is monitored over time[23]. Aspirated spheroids behave like a viscoelastic liquid, first displaying an elastic response followed by an apparently linear viscous response. The constant creep rate $\dot{L}_\infty$ of the linear viscous response during both aspiration and relaxation of the spheroid (once the aspiration pressure is released) is used to calculate the spheroid surface tension γ[23,24]. Intriguingly, γ was shown to depend on the applied aspiration pressure ΔP, suggesting a reinforcement of γ through an active response of the cells to the mechanical force[23]. However, no dependency of γ on the applied force was observed in parallel-plate tensiometry experiments, where spheroids are exposed to a uniaxial compressive strain[17,19]. This raises the question whether cells actively reinforce their surface tension with the applied force or if the current understanding of viscoelastic spheroid aspiration data is insufficient.

In this study, we address this question by investigating how the duration that cells are exposed to different aspiration forces, alongside differences in cell mechanics, affect the tissue surface tension and its possible reinforcement. For this, we used our recently developed microfluidic micropipette aspiration device[25]. We first

[1]Department of Chemical Engineering, Delft University of Technology, Delft 2629, HZ, The Netherlands. [2]Department of Bionanoscience, Kavli Institute of Nanoscience, Delft University of Technology, Delft 2629, HZ, The Netherlands. [3]Department of Cell and Chemical Biology and Oncode Institute, Leiden University Medical Center, Leiden 2333, ZA, The Netherlands. ✉email: p.e.boukany@tudelft.nl

measured the viscoelastic aspiration and relaxation behavior of mice fibroblast spheroids, and demonstrated that their viscoelastic relaxation is both time frame- and deformation-dependent. We then characterized viscoelastic creep for spheroids with different expression levels of alpha-smooth muscle actin, a cytoskeletal protein upregulating cellular contractility, and found that a decrease in spheroid deformability resulted in a slower cellular retraction rate after pressure release. Lastly, our measurements indicated a time frame-dependent cellular retraction, raising the question whether the viscosity and/or surface tension remain constant during this retraction. In order to uncouple the influence of viscosity and surface tension on the measured viscoelastic creep, we aspirated soft HEK293T cell spheroids with a negligible surface tension, and found that here viscosity proved to be pressure-dependent in contrast to previous spheroid studies. Our findings show that spheroid viscoelasticity is deformation-dependent, an essential behavior previously unaccounted for when deriving tissue surface tension, and thus challenge the putative reinforcement of this tension at larger pressures.

Results

Spheroid viscoelastic relaxation is time frame-dependent

Recently, we have developed a microfluidic micropipette aspiration device that allows for a higher throughput in comparison to the conventional glass micropipette technique[25]. Where the traditional technique only aspirates one spheroid at a time, our device can aspirate up to eight spheroids simultaneously (Fig. 1a). By flowing spheroids into individual parallel aspiration pockets that are aligned with squared constriction channels of $50 \times 50\,\mu m^2$ (mimicking micropipettes), parallel creep tests can be applied by lowering a water reservoir attached to the outlet of the device [see "Methods" and Supplementary Fig. S1]. First, a spheroid aspiration measurement is conducted, where the creep length $L(t)$ increases over time. Next, the pressure is released by bringing the reservoir back to the original height, thus starting a stress relaxation test, where the protrusion retracts over time.

By fitting the creep data with a modified Maxwell model[23] and see Supplementary Information], the fast elastic deformation δ at short times and viscous flow with constant velocity $\dot{L}_\infty$ at long times can be defined for both the aspiration and retraction curves. Assuming volume conservation of the non-aspirated part of the spheroid, the aspiration force for a cylindrical pipette is given by $f = \pi R_p^2 (\Delta P - \Delta P_c)$, with R_p the radius of the pipette and ΔP_c the critical pressure above which aspiration occurs[23]. Assuming that the viscosity η of the spheroid remains unchanged during the aspiration and retraction phase, the critical pressure is deduced from $\Delta P_c = \Delta P \dot{L}_\infty^r / (\dot{L}_\infty^r + \dot{L}_\infty^a)$, where $\dot{L}_\infty^r$ and $\dot{L}_\infty^a$ are the retraction and aspiration flow rates, respectively [for full derivation see Supplementary Information]. By applying the Laplace law, the spheroid surface tension is derived from the critical pressure via $\Delta P_c = 2\gamma (\frac{1}{R_p} - \frac{1}{R})$, with R being the radius of the spheroid, which can be approximated by the initial radius of the spheroid R_0, as $R_p \ll R_0$. We correct R_p for the squared constrictions on our microfluidic device, following previous work by Davidson et al.[26,27]. The effective channel radius R_{eff} for our $50 \times 50\,\mu m^2$ channel is 27 μm [for derivation see Supplementary Information].

Homogeneous spheroids of NIH3T3 fibroblast cells and human embryonic kidney (HEK293T) cells were formed using the Sphericalplate 5D (Kugelmeiers) and ranged between 65 and 125 μm in radius through all experiments [see "Methods" and Supplementary Fig. S2]. The microfluidic device was coated with 1% Pluronic® F127 (Sigma) to prevent adhesion of the spheroid tongue to the PDMS constriction walls, and all experiments were performed at 37 °C and 5% CO_2 using a stage top incubator (ibidi). More details on the microfluidic device can be found in our previous study[25] and the "Methods". The bulk of the measurements in this study were performed using NIH3T3 spheroids, which were aspirated at various pressures and durations. Only spheroids with a constant volume during aspiration were analyzed. During the stress relaxation test, bringing ΔP entirely
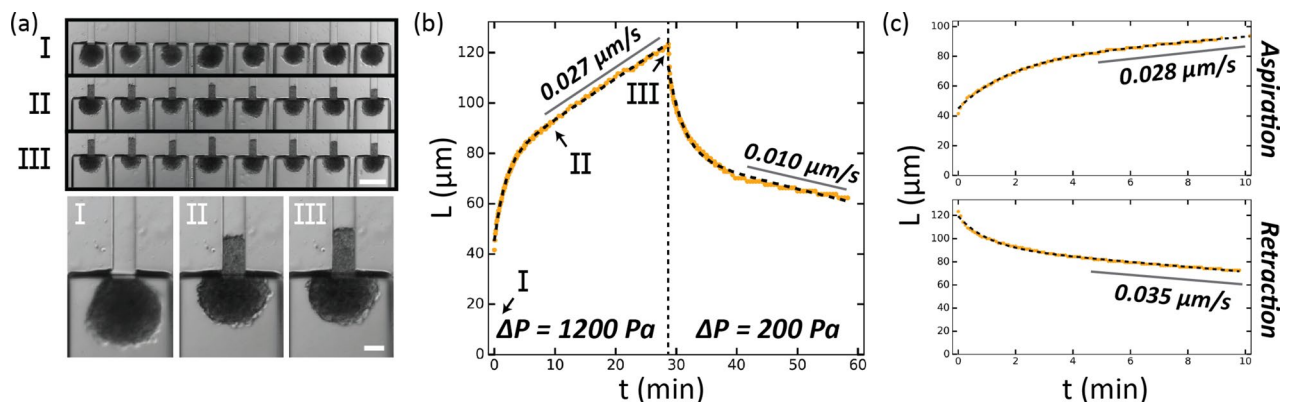

Fig. 1. Tissue viscoelastic relaxation of NIH3T3 fibroblast spheroids is time frame-dependent. (**a**) Brightfield images of 8 NIH3T3 spheroids aspirated at 0 min (I), 10 min (II) and 30 min (III), with an overview of the microfluidic micropipette aspiration chip (top, scale bar 200 μm), and a single spheroid close-up (bottom, scale bar 50 μm). (**b**) The creep length L, being the distance from the spheroid protrusion edge to the start of the constriction channel, plotted versus time for the NIH spheroid [shown in (**a**, bottom)] aspirated at 1200 Pa for 30 min after which the pressure is lowered to a small pressure (200 Pa) and the spheroid is left to retract for 30 min. The data (orange dots) is fitted with the Modified Maxwell model (black dashed lines), and the derived viscous creep rate values for $\dot{L}_\infty^a$ and $\dot{L}_\infty^r$ are added to the plot. (**c**) The first 10 min of the aspiration (top) and retraction (bottom) of the experiment in (**b**), with viscous creep rates derived by only fitting these first 10 min.

back to zero often made spheroids move out of the pockets, preventing the monitoring of the protrusion retraction. This was likely due to the presence of a minor backflow in the microfluidic device, as manually bringing back the outlet reservoir to the exact same starting height proved to be difficult. To circumvent this, all retraction measurements were performed by leaving a minor pressure, $\Delta P = 200$ Pa, that still allowed for the protrusion to retract while keeping it in the constriction channel for monitoring. This led to a small readjustment in the derivation of ΔP_c and γ [Supplementary Information].

First, creep aspiration tests were performed on NIH3T3 spheroids for 30 minutes (min), long enough for the protrusions to have entered the linear viscous regime (as the creep rate did not change anymore after 10 min) (Fig. 1a). Next, stress relaxation tests were captured for an identical 30 min (Fig. 1b). Interestingly, we observed that the duration of retraction strongly influenced the derived viscous retraction flow velocity $\dot{L}^r_\infty$ (Fig. 1c). This observation raised the question whether the time frame for the retraction experiment was long enough to fully capture the linear relaxation. When we performed a 2 h-long retraction measurement, we found that the retraction flow velocity became lower over time as the creep curve plateaued [Supplementary Fig. S3]. Interestingly, in traditional MPA studies on murine sarcoma (S180) cell spheroids, where no remaining pressure was left during retraction, the flow velocity did appear to be linear over time[23,24]. We hypothesize that the minor pressure left in our retraction measurements induced the plateau, which would mean that here retraction is not governed by one constant critical pressure ΔP_c. Instead, the spheroid protrusion first retracts with a large ΔP_c upon release of the aspiration pressure, after which the creep curve plateaus due to the remaining pressure counteracting the spheroid now retracting with a smaller ΔP_c. To eliminate the influence of active contraction on spheroid retraction, we treated the NIH3T3 spheroids with the myosin II inhibitor Blebbistatin and monitored their retraction at 200 Pa. Now, the spheroids first displayed a minor elastic retraction after which they started aspirating again [see "Methods" and Supplementary Fig. S4]. This observation also challenges the assumption held in literature[23,24,28] that spheroid retraction is governed by a constant ΔP_c, as here retraction changed into aspiration over time. We therefore hypothesize that spheroid retraction is determined by an interplay between retractile cellular elastic properties and the viscous flow of the spheroid tongue as a cellular collective, each having their own critical pressure inducing retraction.

Spheroid viscoelastic relaxation is deformation-dependent

To test whether we observe a reinforcement in γ for increasing ΔP as reported in Ref.[23], measurements with NIH3T3 spheroids were conducted using two slightly differing aspiration pressures (1000 Pa and 1200 Pa). Additionally, measurements with a large pressure of 2000 Pa were performed, now for only 10 min of aspiration followed by 10 min of retraction at 200 Pa, as spheroid volumes were not conserved for aspiration times beyond 10 min. At 1000 and 1200 Pa, we observed pulsed contractions or "shivering" in approximately half of the aspiration curves [Supplementary Fig. S5], resembling observations reported with glass micropipette aspiration measurements by Guevorkian et al.[29]. This shivering effect did not occur at the large pressure of 2000 Pa, where the protrusion flowed smoothly in the constriction. Despite the shivering, aspiration curves could still be fitted with the modified Maxwell model and retraction curves were comparable for spheroids that did or did not shiver during aspiration [Supplementary Table S1]. The small influence of shivering on $\dot{L}^a_\infty$ did not significantly influence $\dot{L}^r_\infty$ nor γ for different conditions, so we included these data. For the three different aspiration pressures, we indeed observed an apparent force-dependent γ, where the derived surface tension increased for larger ΔP (Fig. 2a). Accordingly, the stress relaxation curves demonstrated an increase in retraction flow velocity $\dot{L}^r_\infty$ for larger ΔP (Fig. 2b), which was similarly observed in glass micropipette aspiration experiments[23]. Previously, this was interpreted as the spheroid protrusion actively mechanosensing the magnitude of the aspiration force, causing it to reinforce and retract faster. However, as demonstrated in Fig. 1b,c, $\dot{L}^r_\infty$ depends on the time frame during which the relaxation is investigated. Intriguingly, when fitting only the first 10 min of retraction for the measurement at 1000 Pa, we find that the average $\dot{L}^r_\infty$ at 1000 and 2000 Pa is the same [Fig. 2b, right-side]. While the total deformation length L_{max} of the spheroid protrusion at the end of aspiration is understandably larger when aspirating for 30 min at 1200 Pa compared to 1000 Pa, we find that the same average length has been reached when aspirating for 30 min at 1000 Pa or 10 min at 2000 Pa, indicating a deformation-dependency for retraction (Fig. 2c). Indeed, we find that $\dot{L}^r_\infty$ is linearly dependent on L_{max}, where the further the protrusion has reached after aspiration, the faster it retracts when comparing identical time frames [Fig. 2d, Supplementary Fig. S6 (1000 Pa and 2000 Pa)]. In addition, a larger aspiration flow velocity $\dot{L}^a_\infty$ results in a larger L_{max} and thus larger $\dot{L}^r_\infty$ [Supplementary Fig. S7]. While these trends were observed for the measurements at 1000 and 1200 Pa, they were not significant for the measurements at 2000 Pa, likely because of the larger standard deviation in $\dot{L}^r_\infty$ at the short timescale of 10 min, alongside the smaller range in L_{max} and the smaller number of data points. Altogether, for our measurements at 1000 and 1200 Pa, we show that $\dot{L}^r_\infty$ and the derived γ do not solely depend on either the applied force or time frame but directly relate to the product of both, being the resulting length of deformation L_{max}.

Derived tissue surface tension is not influenced by spheroid deformability

What cellular properties govern retraction flow velocity and its deformation-dependency is unclear. We therefore sought to investigate the influence of spheroid deformability on the retraction flow and spheroid viscoelasticity. Alpha-smooth muscle actin (α-SMA), the mesenchymal marker and cytoskeletal protein that is incorporated into stress fibers of fibroblasts, upregulates their contractile activity and ability to remodel tissues[30–32]. We found that increasing the NIH3T3 cell seeding density during fabrication strongly influenced the α-SMA expression in our spheroids (Fig. 3a,b). Immunostaining and Western blots analysis showed that doubling the cell seeding density from 1.5×10^6 (used in Fig. 2) to 3×10^6 cells increased the average protein expression of α-SMA by a factor of 6 (Fig. 3c). We hypothesize that cells differentiated at higher density, similar to fibroblasts increasing
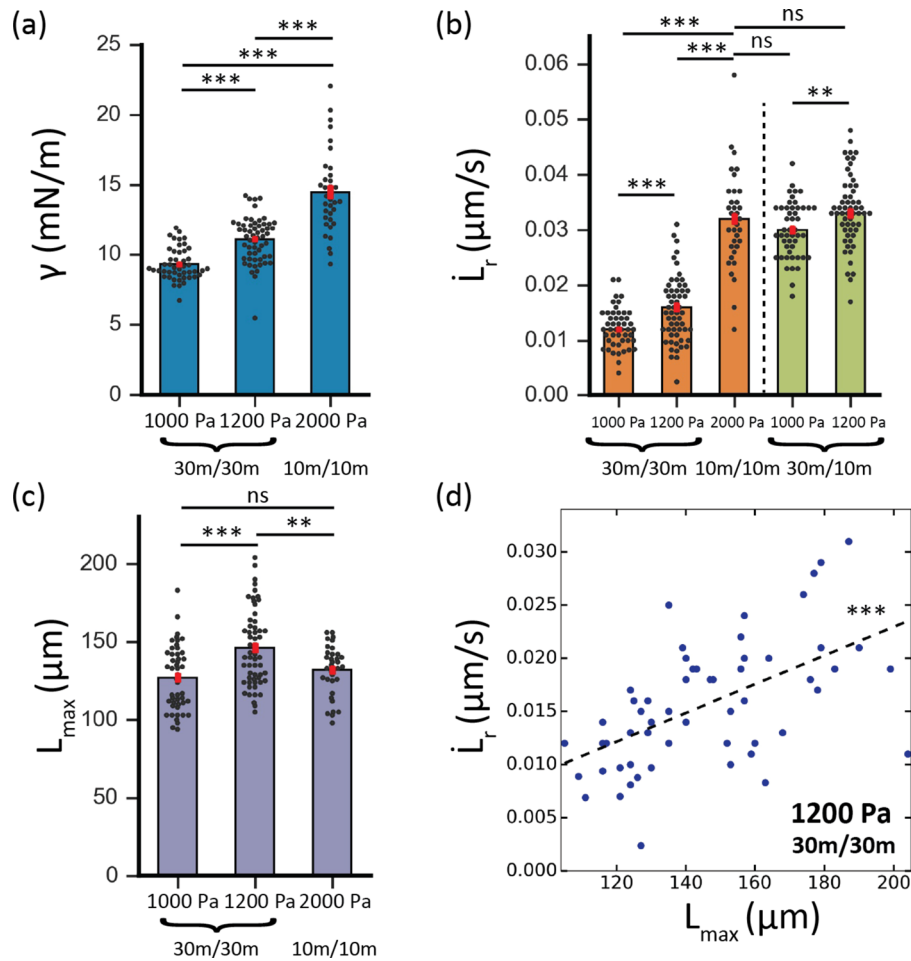
Fig. 2. Tissue relaxation behavior is deformation-dependent. (**a**–**c**) Histograms comparing mechanical parameters for NIH3T3 spheroids aspirated at 1000 Pa (30 min aspiration, 30 min retraction, n = 48), at 1200 Pa (30 min aspiration, 30 min retraction, n = 57), and at 2000 Pa (10 min aspiration, 10 min retraction, n = 35). Retraction was performed at a remaining pressure of 200 Pa. (**a**) The tissue surface tension γ, (**b**) retraction flow velocity $\dot{L}^r_\infty$ and (**c**) resulting creep length at the end of the aspiration L_{max} are compared. For (**b**), the two green bars on the right of the dotted line depict the derived $\dot{L}^r_\infty$ when only fitting the first 10 min of retraction. (**d**) The retraction flow velocity $\dot{L}^r_\infty$ plotted versus L_{max} for NIH3T3 spheroids aspirated at 1200 Pa (30 min aspiration, 30 min retraction). **p < 0.01, ***p < 0.001 and ns is nonsignificant. Error bars are SEM.

their α-SMA expression in response to the cytokine TGF-β 1 when seeded at a larger cell density in 2D[33]. Identical to the previous spheroids, we aspirated the 3×10^6 cell spheroids at 1200 Pa for 30 min and then let them retract at 200 Pa for 30 min. Our results showed that spheroid surface tension γ did not change, despite the higher expression of α-SMA (Fig. 3d). This was unexpected, as the 3×10^6 cell spheroids reached less far in the constrictions, demonstrating a smaller deformability (Fig. 3e). Additionally, their viscous flow rate $\dot{L}^a_\infty$ was significantly slower, as was their $\dot{L}^r_\infty$ (Fig. 3f,g). This is in agreement with Fig. 2d, where the spheroid tongues that deformed less also retracted slower. We calculate that the 3×10^6 cell spheroids have a higher average viscosity of $\eta = 150 \pm 9$ kPa s in comparison to the 1.5×10^6 cell spheroids with $\eta = 68 \pm 3$ kPa s [derived as explained in Supplementary Information], explaining their different deformability at the same critical pressure ΔP_c.

Previous measurements with parallel-plate tensiometry on spheroids composed of different cell lines showed a linear correlation between bulk viscosity and surface tension[34]. In contrast, our microfluidic measurements show that a larger viscosity does not affect surface tension. However, our findings on a time frame-dependent retraction raise the question whether the viscosity and/or ΔP_c remain constant during MPA retraction. If this assumption would prove to be incorrect, disentangling η and γ when interpreting the measured $\dot{L}^a_\infty$ and $\dot{L}^r_\infty$ becomes very difficult, as we are left with two separate responses (aspiration and retraction) each with two unknown variables.

Viscosity is pressure-dependent for soft spheroids

To untangle η and γ, we investigated the viscous flow behavior of spheroid aspiration and retraction without the influence of ΔP_c, using human embryonic kidney (HEK293T) cell spheroids with a very low surface tension (Fig. 4a). In order for the spheroid volume to remain unchanged during the measurements, we aspirated the HEK293T cell spheroids for 5 min at two different pressures of 200 Pa and 500 Pa. We then monitored
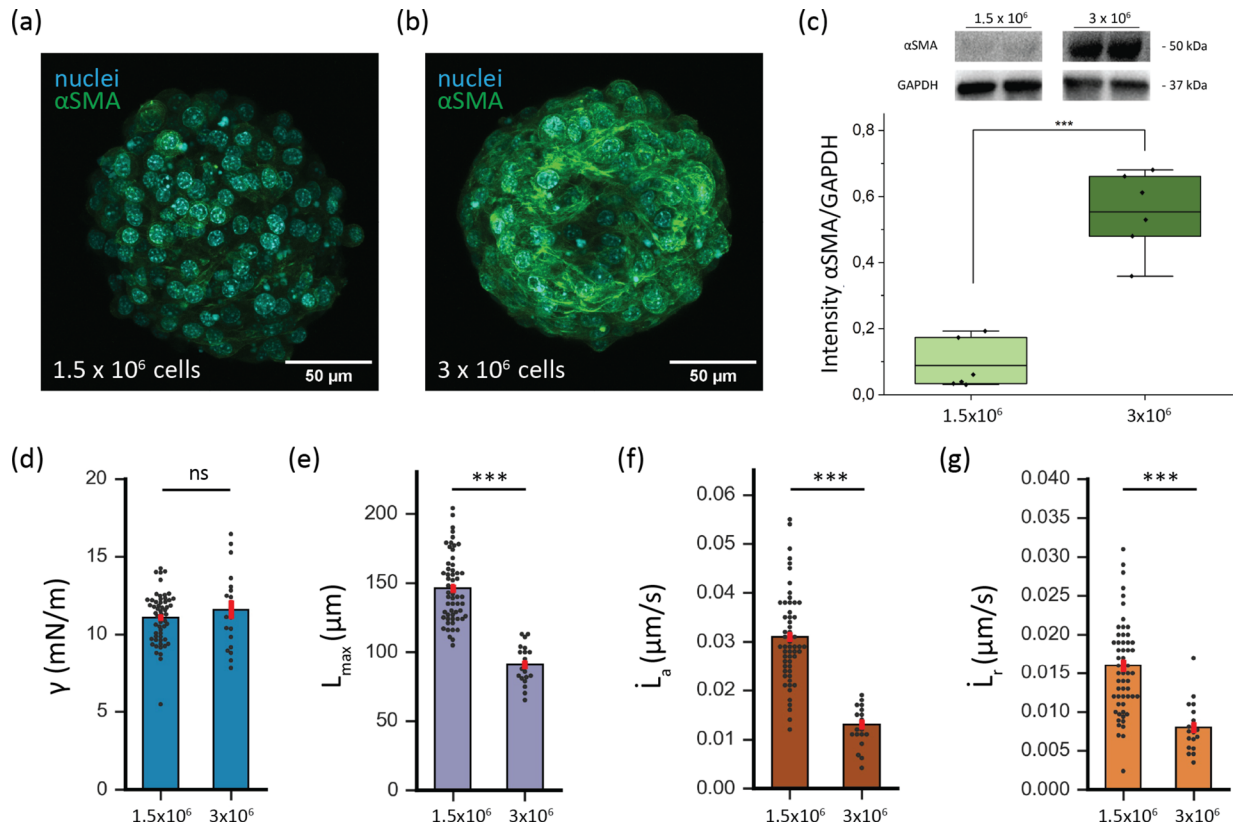
Fig. 3. A higher expression of α-SMA does not influence derived tissue surface tension. (**a, b**) Max intensity confocal fluorescent images of nuclei (cyan) and α-SMA (green) in NIH3T3 spheroids seeded with (**a**) 1.5×10^6 cells/well and (**b**) 3×10^6 cells/well. (**c**) Relative protein levels of α-SMA in respect to GAPDH for NIH3T3 spheroids seeded with 1.5×10^6 and 3×10^6 cells/well. Blot insets are independent samples for the two different seeding densities, run on and cropped from different parts of the same gel. Each seeding density sample was run for both α-SMA and GAPDH on different parts of the same gel, with original blots presented in Supplementary Fig. S8. (**d–g**) Histograms comparing mechanical parameters for NIH3T3 spheroids aspirated at 1200 Pa at a seeding density of 1.5×10^6 cells (30 min aspiration, 30 min retraction, n = 57) and a seeding density of 3×10^6 cells (30 min aspiration, 30 min retraction, n = 19). Retraction was performed at a remaining pressure of 200 Pa. (**d**) The tissue surface tension γ, (**e**) resulting creep length at the end of the aspiration L_{max}, (**f**) aspiration flow velocity $\dot{L}_\infty^a$ and (**g**) retraction flow velocity $\dot{L}_\infty^r$ are compared. ***p < 0.001 and ns is nonsignificant. Error bars in histograms are SEM.
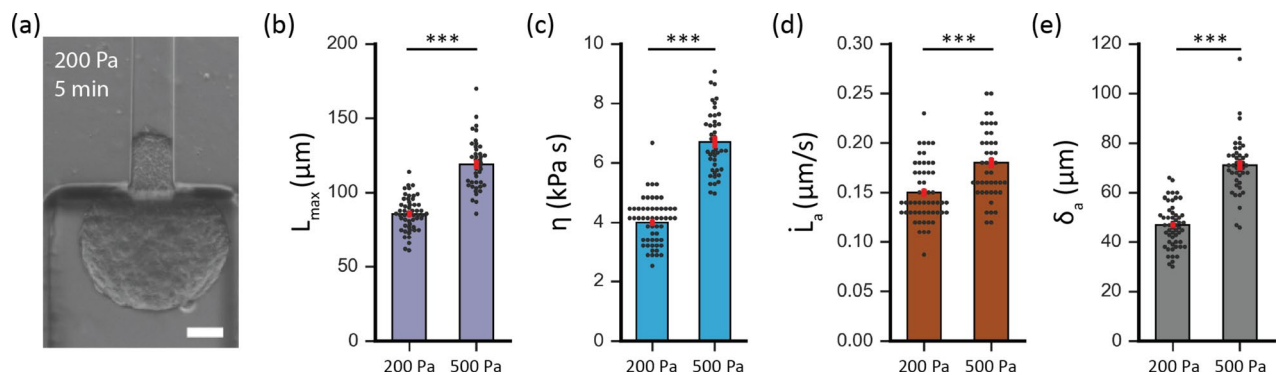

Fig. 4. For soft HEK293T cell spheroids, viscosity is pressure-dependent. (**a**) Brightfield image of a HEK293T cell spheroid after 5 min of aspiration at 200 Pa. Scale bar 50 μm. (**b–e**) Histograms comparing mechanical parameters for HEK293T spheroids aspirated at 200 Pa (5 min aspiration, 5 min retraction, n = 54) and at 500 Pa (5 min aspiration, 5 min retraction, n = 43). Retraction was performed at a remaining pressure of 50 Pa. (**b**) The viscosity η, (**c**) resulting creep length at the end of the aspiration L_{max}, (**d**) aspiration flow velocity $\dot{L}_\infty^a$ and (**e**) elastic deformation length during aspiration δ_a are compared. ***p < 0.001. Error bars are SEM.

retraction for 5 min at a remaining minor pressure of 50 Pa. After 200 Pa aspiration, spheroid tongues retracted elastically and then started aspirating again, indicating that their ΔP_c during viscous retraction was indeed minimal (below 50 Pa) [Supplementary Fig. S9]. Upon 500 Pa aspiration, spheroid tongues deformed further into the constrictions (Fig. 4b) and now displayed a linear viscous retraction over time, resulting in an average $\gamma = 1.9 \pm 0.1$ mN/m. This behavior is again consistent with a deformation-dependent retraction, although it could also still be explained by a potential reinforcement in γ at larger pressures. Importantly, we find for HEK293T cell spheroids that their measured viscosity at low pressures is pressure-dependent (Fig. 4c). This contrasts with our measurements for stiffer NIH3T3 spheroids, where the viscosity was pressure-independent (Supplementary Fig. S10a), similar to the previous study by Guevorkian et al. with S180 cell spheroids[23]. In our own previous study with a slightly different microfluidic design (aspiration pockets were rounded instead of rectangular)[25], we aspirated HEK293T spheroids at 500 and 700 Pa and also showed their viscosity to be pressure-independent. We believe that the discrepancy with our new data can be explained by the smaller pressure range (factor 1.4, compared to a factor 2.5 in the current work) and the larger standard deviation in L_∞^a for our previous microfluidic device. Our new measurements on HEK293T spheroids clearly displayed a significant increase in η when raising the pressure, from $\eta = 4.0 \pm 0.1$ kPa s at 200 Pa to $\eta = 6.7 \pm 0.2$ kPa s at 500 Pa (Fig. 4c). For 200 Pa, we calculated the viscosity by assuming $\Delta P_c = 0$ Pa, thus giving an upper bound for η, and calculated the viscosity at 500 Pa via our derived ΔP_c from L_∞^a and L_∞^r. Though at 500 Pa the spheroid protrusion flows faster than at 200 Pa (Fig. 4d), the proportional change in L_∞^a is much smaller than the 2.5-fold increase in pressure, translating to a larger viscosity at 500 Pa. Also, the proportional change in the initial elastic deformation δ_a during aspiration is larger than the change in L_∞^a between the two pressures (Fig. 4e). These results indicate that an increase in aspiration force results in a larger proportional change in the elastic deformation than in the viscous flow of cells during aspiration. Interestingly, we also find a pressure-dependent η for our NIH3T3 spheroid measurements when we reanalyze the data, neglecting the increase in L_∞^r and using that ΔP_c is the same at 1000 Pa and 1200 Pa (Supplementary Fig. S10a). Similar to the HEK293T measurements, the increase in force induces a larger proportional change in δ_a than for L_∞^a [Supplementary Fig. S10b,c]. This implies that another possible framework exists besides tissue surface tension reinforcement, in which not surface tension but spheroid viscosity is pressure-dependent for MPA measurements. In that case, either η or ΔP_c is different between aspiration and retraction, as the flow velocity is deformation-dependent during retraction.

Discussion

In this study, we have measured a force-dependent spheroid surface tension γ coupled to an increased viscous flow rate L_∞^r at larger deformations. The reinforcement of γ with applied force has previously been explained by an active response of cells to mechanical forces, involving cytoskeletal remodeling potentially due to stress fiber polymerization by myosin II motors, stretch-activated membrane channels or the clustering of cadherins[23,35–40]. Next to this, spheroid surface tension has also previously been coupled to the size of spheroids[24], where spheroids in the size range of 160–360 μm in diameter displayed a smaller γ as the size increased. Unfortunately, the size range that our microfluidic device can aspirate was too small to reproduce this effect [Supplementary Fig. S11]. However, our results have generated new insights in the viscoelastic behavior of spheroids during MPA and the interpretation of γ thanks to the large amount of data we could obtain by high-throughput microfluidic aspiration (Fig. 5). We found that the retraction flow velocity L_∞^r changed over time when leaving a minor pressure, indicating a non-constant ΔP_c that is governed by different components with different timescales. Additionally, the retraction velocity correlated with the total deformation L_{max} at the end of aspiration throughout all measurements, with a larger deformation resulting in a faster retraction. Similarly, more viscous spheroids with a smaller L_{max} retracted slower despite their lowered deformability, resulting in an unchanged surface tension γ and thereby disagreeing with previous parallel-plate tensiometry experiments, which showed a linear correlation between viscosity and surface tension[34]. Finally, for soft HEK293T cell spheroids, retraction flow only occurred for larger deformations, despite an increase in viscosity at larger pressures. We therefore propose a different framework than tissue surface tension reinforcing with applied force to interpret viscoelastic spheroid MPA data, in which L_∞^r is governed by the total deformation L_{max}. For this framework, simply running an aspiration measurement for a longer time would not affect the viscosity and critical pressure during aspiration, but result in a larger L_{max}, L_∞^r and thus lower viscosity or larger critical pressure during retraction. Therefore, η and/or ΔP_c would be different between aspiration and retraction.

How to distinguish tissue surface tension and viscosity from each other during aspiration measurements, and how to identify whether γ, η or both are pressure-dependent during MPA remains an open question. Previous studies have shown how the liquid-like properties of cellular tissues are determined by tissue flow via cells rearranging and slipping past each other[13,14,41–44]. In an experiment with mCherry-transfected NIH3T3 cells and a microfluidic device modified to allow detailed imaging in the constriction channel, we did not observe cells slipping past each other in the constriction channel, demonstrating that the viscous flow was unlikely to be governed by cell rearrangements [see Supplementary Movies S1 and S2, and "Methods" for the device modifications]. We hypothesize that the deformation-dependent viscoelasticity can be explained by the number of individual cells that have been aspirated into the constriction channel. If each cell has its own relaxation rate, then a spheroid protrusion with more cells in series will have a larger L_∞^r, being the sum of all these individual cellular retraction rates. Yet, how the tissues' effective viscosity is precisely governed at the cellular level, and how different cytoskeletal elastic and viscous components work over different timescales to govern ΔP_c remains to be examined. Overall, we show that spheroid viscoelastic behavior is pressure- and deformation-dependent for MPA, challenging the assumption that both η and ΔP_c are identical during aspiration and retraction.
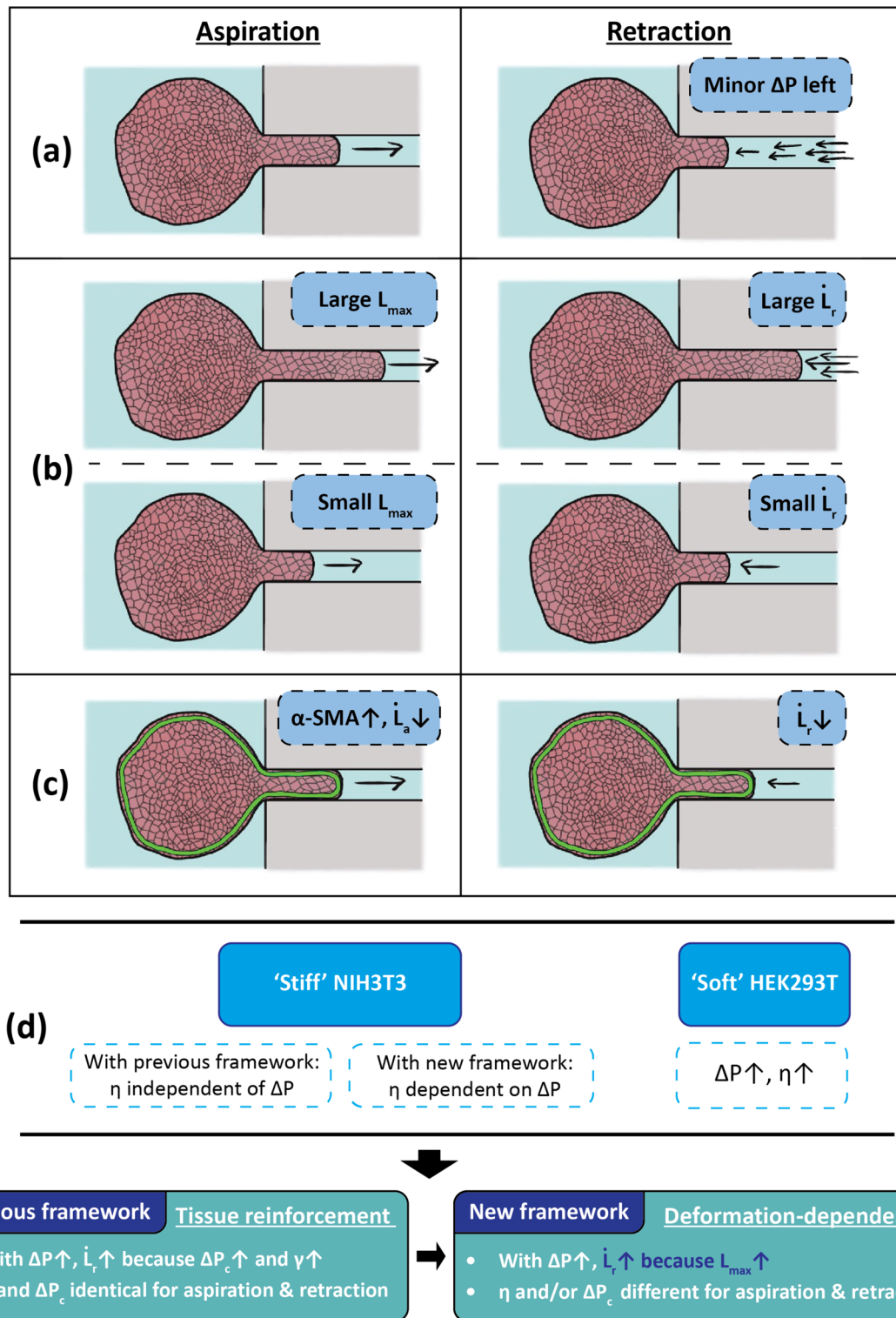
Fig. 5. Main findings of the study. (**a**) The retraction rate $L^{\dot{r}}_{\infty}$ of the spheroid protrusion changes over time when leaving a minor pressure ΔP during retraction. (**b**) The retraction rate $L^{\dot{r}}_{\infty}$ is deformation-dependent, with larger deformations leading to a larger retraction rate. (**c**) Decreasing spheroid deformability through a higher expression of α-SMA leads to a decreased retraction rate $L^{\dot{r}}_{\infty}$. (**d**) For 'soft' HEK293T cell spheroids, viscosity η is pressure-dependent. When assuming critical pressure ΔP_c during aspiration to be independent of applied pressure ΔP, η is also pressure-dependent for 'stiff' NIH3T3 cell spheroids. Through these findings, we propose a new framework to explain spheroid viscoelastic behavior, where the viscosity η and/or critical pressure ΔP_c differ between aspiration and retraction.

Methods

Cell culture

NIH3T3 embryonic mouse fibroblasts (ATCC CRL-1658) were kept in Dulbecco's Modified Eagle Medium (DMEM, Gibco) containing 4.5 g L^{-1} glucose, L-glutamine, without sodium pyruvate, and supplemented with 10% Newborn Calf Serum (NCS, Gibco) and 1% antibiotic-antimycotic solution (Sigma-Aldrich). Transfected LifeAct-GFP_NLS mCherry NIH3T3 cells, used for the Supplementary videos, were cultured in Dulbecco's Modified Eagle's Medium (DMEM, Thermo Fisher Scientific), supplemented with 10% Fetal Bovine Serum (FBS, Thermo Fisher Scientific), 1% penicillin/streptomycin (Pen/Strep, Thermo Fisher Scientific), and 1 µg/ml of Puromycin (Thermo Fisher Scientific).

Human embryonic kidney 293T (HEK293T, DSMZ, ACC 635) cells were kept in DMEM/F12 with GlutaMAX (Gibco), supplemented with 10% Fetal Bovine Serum (FBS, Sigma) and 1% penicillin-streptomycin solution (Gibco).

All cells were incubated at 37 °C with 5% CO_2 in TC T-25 or T-75 flasks (Sarstedt), and subcultured at least twice a week, until a maximum passage number of 30. Cells were periodically checked for mycoplasm.

Cell transfection with NLS-mCherry and LifeAct-GFP for Supplementary videos

The pCDNA_Lifeact-GFP_NLS-mcherry was a gift from Olivier Pertz (Addgene plasmid #69058). From this vector, a SmaI-EcoRV fragment containing the NLS-mCHERRY ORF was cloned in the HpaI site of the pLV-CMV-IRES-PURO vector. Next, the EF1a promoter, from pcDEF3, was cloned in the BstZ17I site of pLV-PURO-NLS-mCHERRY. Finally, the NdeI-HincII fragment, containing LifeAct-GFP (from pCDNA_Lifeact-GFP_NLS-mCherry), was cloned in the NdeI-EcoRV sites.

Lentiviruses were produced by co-transfecting cDNA expression plasmids with helper plasmids pCMV-VSVG, pMDLg-RRE (gag/pol), and pRSV-REV into HEK293T cells using polyethyleneimine (PEI). Cell supernatants were harvested 48 hours after transfection and stored at −80 °C. NIH3T3 cells were labelled by infecting for 24 hours with LifeAct-GFP_NLS mCherry expressing lentiviral supernatants diluted 1:1 with cell culture medium and 5 ng/ml of polybrene (Sigma-Aldrich). Forty-eight hours after infection, cells were placed under Puromycin (Thermo Fisher Scientific) selection. Cells were cultured with 1 µg/ml of Puromycin to obtain a stable fluorescent cell line and maintain selection pressure.

Spheroid preparation

Spheroids were fabricated using the Sphericalplate 5D (Kugelmeiers), a 24-well cell culture plate with 12 functional wells each containing 750 microwells. Depending on the desired NIH3T3 cell spheroid size, cell suspensions with seeding densities ranging between 1.5 and 3×10^6 cells, determined with a TC20TM automated cell counter (Bio-Rad), were obtained through trypsinization with 0.25% trypsin-EDTA (Gibco), and subsequently deposited in a functional well to form spheroids. For HEK293T cell spheroids, a total of 0.75×10^6 cells was seeded in the well. All cells were deposited in a total final volume of 2 mL of corresponding cell media. After deposition, cells sediment in the microwells due to gravity and aggregate into spheroids. The resulting spheroid dimensions depended on the initial cell seeding density, which was observed both by eye and from images taken right before running the MPA experiments. All cell spheroids were cultured in the wells for 2 days before aspiration experiments, and the media was refreshed every day. On the day of the experiment, a spheroid suspension was generated by gently washing the spheroids out of the microwells using the culture media already present in the well, and finally taking out 1 mL of this same media with suspended spheroids.

Immunocytochemistry

Bovine type I collagen 2.4 mg/mL (reported purity ≥ 99.9%, Advanced Biomatrix) was prepared for 3D hydrogels as described in the protocol provided by Advanced Biomatrix. The collagen gel was polymerized in µ-Slide 8 well chambers (ibidi) for 45 min at 37 °C. NIH3T3 spheroids were pipetted on top of the collagen gels and incubated for 30 min at 37 °C and 5% CO_2 to ensure attachment. Medium was removed from the wells and the spheroids were fixated with 4% formaldehyde (Thermo Fisher Scientific) in phosphate buffered saline (PBS, Sigma-Aldrich) for 10 min. After fixation, the spheroids were washed three times with PBS and permeabilized with 0.5% Triton-x 100 (Sigma-Aldrich) in PBS for 3 min. Spheroids were blocked overnight in 3% bovine serum albumin (BSA, Sigma Aldrich) in PBS with 0.1% Tween 20 (PBST, Sigma-Aldrich) at 4 °C. The next day, spheroids were incubated overnight with mouse anti-alpha-smooth muscle actin 1:500 (A257, Sigma-Aldrich) in 1.5% BSA/PBST at 4 °C. After incubation, spheroids were washed three times with PBST and incubated with goat anti-mouse 568 (a1105, Thermo Fisher Scientific) 1:1000 and Hoechst 33342 (Thermo Fisher Scientific) 1:1000 in PBST for 4 h at room temperature. After secondary incubation, spheroids were washed three times with PBST. The spheroids were imaged on a Stellaris 8 confocal microscope (Leica), equipped with a supercontinuum white light laser, 405 nm laser and three hybrid detectors. Imaging was performed with the 405 nm laser, a 568 nm laser line and a 20×/0.75 air objective. For both seeding conditions of 1.5 and 3 million cells, three biological replicates were made that were all used for two technical replicates, resulting in n = 6 for each condition.

Western blotting

Spheroids were transferred to Eppendorf tubes and lysed in cold radioimmunoprecipitation buffer (RIPA, Thermo Fisher Scientific). Lysed samples were agitated at 4 °C for 3 h , sonicated with a bath sonicator (Branson 2510 Ultrasonic Cleaner, Marshall Scientific) for 30 s and stored at −20 °C. Laemmli buffer (Bio-Rad) and 4% beta-mercaptoethanol (Sigma) were added to the lysed samples and heated at 95 °C for 5 min. SDS-PAGE was performed with Mini-PROTEAN TGX gels (Bio-Rad) using 120V for 80 min. Western Blot was executed with a Trans-Blot Turbo Transfer System (Bio-Rad) and Trans-Blot Turbo Mini 0.2 µm PVDF Transfer Packs

(Bio-Rad) and membranes were blocked in 5% Bovine Serum Albumin (BSA, Thermo Fisher Scientific) in PBS overnight. Membranes were stained with primary antibodies: mouse anti-alpha smooth muscle actin (#A257, Sigma-Aldrich) 1:500 and rabbit anti-GAPDH (#CST2118S, Bioke) 1:1000 in 5% BSA overnight on a shaker at 4 °C. Membranes were washed thrice with 0.1% Tween (Sigma-Aldrich) in PSB (PSBT) on a shaker, and incubated for 3 hours with secondary antibodies: rabbit anti-mouse HRP (#ab97051, Abcam) 1:5000 and goat anti-rabbit HRP (#ab6728, Abcam) 1:5000 in PBST. Afterwards, membranes were washed thrice with PBST and imaged with an enhanced luminol-based chemiluminescent substrate kit (Thermo Fisher Scientific) on a gel imager (Bio-Rad). For each seeding condition (1.5 and 3 million cells), two biological replicates were made (n = 2). Signal intensities of α-SMA and GAPDH bands were measured in ImageJ with three regions of interest (ROIs), each subtracted from different background spots in the corresponding lane, resulting in six datapoints for each condition. To compare relative α-SMA protein levels between cells, α-SMA band intensities were normalized to corresponding GAPDH band intensities.

Blebbistatin treatment
Myosin II inhibitor (−) Blebbistatin (Abcam) was dissolved in dimethyl sulfoxide (DMSO) at a stock concentration of 5 mM. Spheroids were incubated in a dilution concentration of 10 µm for at least 3 h before experiments.

Fabrication of microfluidic aspiration device
The microfluidic micropipette aspiration chip used in this study is an updated version of the chip introduced in our previous study[25]. In contrast to the previous design with round spheroid aspiration pockets, the pockets in this study were squares to minimize the contact area between the spheroids and the walls of the pockets [Supplementary Fig. S1a]. The updated design is available at: https://github.com/RubenBoot/HighThroughput_Spheroid_MPA. The multi-layered design contains features with different heights, which were created in two separate photolithography steps using a µMLA laserwriter (Heidelberg Instruments). The final chip was designed as a combination of two slabs of crosslinked polydimethylsiloxane (PDMS) (Sylgard 184, Dow Corning); one slab containing the aspiration channels of 50 µm in height plus the top half of the aspiration pockets, and the other slab having the bottom half of the aspiration pockets. The first layer was created by spinning SU-8 3050 (Kayaku Advanced Materials) to an average thickness of 50 µm. For this, the SU-8 was first spun at 500 rpm for 10 s with an acceleration of 100 rpm per s and then at 3500 rpm for 30 s with an acceleration of 300 rpm per s. Subsequently, the SU-8 was soft baked at 95 °C for 15 min, after which the laserwriter wrote the first layer. The wafer was post baked at 65 °C for 1 min, then at 95 °C for 5 min and developed in SU-8 developer (Propylene glycol monomethyl ether acetate (PGMEA), Sigma-Aldrich). The second layer was created with SU-8 2050 (Kayaku Advanced Materials), and spun to an average thickness of 170 µm. For this height, the SU-8 was first spun at 500 rpm for 10 s with an acceleration of 100 rpm per s. Then, it was spun for 30 s with an acceleration of 300 rpm per s at 1100 rpm. The thickness was slightly unequal across the whole wafer, as the resist covered both the first half of the pockets from the first layer as well as the empty spot where the other half of the pockets in the second layer would be written. Therefore, one half of the aspiration pockets including the aspiration channel resulted in a thickness of 176 ± 9 µm while the other half of the pocket had a different thickness of 160 ± 20 µm. After spinning, the wafer was soft baked at 65 °C for 5 min and then at 95 °C for 30 min. The laserwriter wrote the second part of the design, after which the wafer was post baked at 65 °C for 5 min, then at 95 °C for 12 min and then developed again.

The master wafer was coated with trichloro(1H,1H,2H,2H-perfluorooctyl)silane to allow for easy demolding, and PDMS chips were created using Sylgard 184 at a curing agent ratio of 10:1. Individual chips were cut and 2 mm holes were punched in only one slab of the design for the introduction of tubing using a revolving punch plier (Knipex). To facilitate bonding, both halves of the design were plasma cleaned (Harrick Plasma) for two and a half minutes at 30 W, after which one half was slightly wetted with a droplet of distilled water to aid the alignment. The two halves were aligned with the help of the alignment arrows at the border of the design and by using an optical microscope (ZEISS Primovert) to check the alignment. Finally, the chips were kept in the oven at 65 °C to bond overnight. After fabrication, they could be stored indefinitely and used on the desired day for experiments.

Modification of microfluidic chip for Supplementary Movies S1 and S2
When imaging cells inside the microfluidic device consisting out of two bonded PDMS slabs, we could only get the cells in focus with the 5x/NA 0.16 air objective of our inverted fluorescence microscope using an excitation wavelength of 587 nm and an emission wavelength of 610 nm (Zeiss Axio-Observer). As we needed higher resolution to observe individual cells moving in the constriction channel for Movies S1 and S2, we created a modified chip by bonding only the PDMS slab including the constriction channel directly to a glass coverslip. This modified chip was only 175 µm high, with the constriction channel positioned at the bottom of the device. The experiment in Movies S1 and S2 therefore does not represent exactly the same aspiration and retraction conditions as in the rest of the experiments performed in this study, but it does provide valuable insights into the movement of cells within the constriction during aspiration of spheroids.

Microfluidic aspiration data acquisition
The microfluidic aspiration data was acquired following a similar protocol as in our previous study[25]. To prevent cell adhesion to the PDMS walls, the chip was coated before each experiment with 1% Pluronic® F127 (Sigma) in PBS (Gibco) solution and left at room temperature. After 45 min, the Pluronic solution was flushed from the chip using the culture medium that matched the cell line used in the experiment. Vials with cell-free culture media were connected to the inlet and outlet of the microfluidic chip using PTFE 008T16-030-200 tubing (Diba

Industries, inner diameter 0.3 mm, outer diameter 1.6 mm) and a pressure was applied to the media with a MFCS-EZ pressure controller (Fluigent). After the Pluronic solution, small PDMS debris and possible air bubbles were flushed out, the tube connected to the inlet was gently unplugged from the chip, and a loading reservoir, being a shortened 1 ml pipette tip cut with a scalpel, was plugged into the inlet. Then, the vial connected to the outlet was disconnected from the pressure controller and mounted to a vertical translation stage (Thorlabs, VAP10) with a ruler on the side where the pressure in terms of cmH_2O could be read off from. The average human error in reading off the pressure was defined by the thickness of the lines on the ruler indicating the distances, which was $0.2\,cmH_2O$ (~ 20 Pa). This allowed us to exert a precise hydrostatic aspiration pressure when lowering the stage with the vial compared to the height of the reservoir [Supplementary Fig. S1b]. Slightly lowering the stage induced a minor flow in the chip towards the aspiration pockets, after which $20\,\mu L$ of spheroid suspension was pipetted into the reservoir. Guided by the flow, spheroids entered the aspiration pockets, after which the outlet tube was brought back to the original height to stop the flow again. Once ready to perform the experiment, the vial was manually lowered to the chosen aspiration pressure, thereby inducing spheroid tongue aspiration. The inlet reservoir volume remained constant during the duration of the experiment, confirming that there was no leakage at the corners of the squared aspiration channels and spheroids fully blocked the channels. A clear flow was visible in the constriction channel whenever a spheroid did not fully block it, and the rare experiments where this occurred were not used for analysis.

Brightfield images of spheroid protrusions entering the constriction channels were captured on an inverted fluorescence microscope (Zeiss Axio-Observer) using a 5x/NA 0.16 air objective and ORCA Flash 4.0 V2 (Hamamatsu) digital camera with a resolution of $2048 \times 2048\,px^2$. The NIH3T3 spheroids were imaged every 5 s for 10 min (for the short 10 min measurements at 2000 Pa) and then every 30 s for a remainder of 20 min (when doing a 30 min measurement at 1000 or 1200 Pa). The much softer HEK293T spheroids were imaged every 5 s for 5 min. We ensured that the full aspiration curve of the tongue was captured by starting the image acquisition before lowering the outlet tube. After the aspiration measurement, a retraction measurement was started by increasing the height of the outlet vial back to a remaining $2\,cmH_2O$ of aspiration pressure to keep the spheroids in the pockets while the protrusion tongues retract. For the HEK293T spheroids, a remaining pressure of $0.5\,cmH_2O$ was maintained during retraction. The retraction measurement was captured using the same conditions as for the aspiration measurement. Only for Supplementary Fig. S3, NIH3T3 cell spheroids were aspirated for 30 min at 1000 Pa, and then left to retract for 2 hours at 200 Pa, from which the first 10 min an image was captured every 5 s and then for the next 110 min every 30 s. At the end of the experiment, spheroids were pushed out of the pockets and flown back towards the inlet by raising the outlet vial above the reservoir. There, the spheroids were removed from the chip by pipetting them up through the reservoir. This way, new spheroids could be inserted to start a new measurement with the same chip. All experiments were conducted at $37\,°C$ and 5% CO_2 using a stage top incubator (ibidi GmbH). Chips were used for multiple successive runs and were always discarded at the end of the day.

Modification for acquisition of Supplementary Movies S1 and S2
For both Supplementary Movies, we recorded the experiment using a $40\times$/NA 1.3 oil objective with the same inverted fluorescence microscope. For Movie S1, we started recording after ±10 min of aspiration at 1000 Pa to capture the viscous retraction, and took an image every 10 s for 20 min. For the retraction in movie S2, we also took an image every 10 s for 20 min at a remaining pressure of 200 Pa. Both movies with mCherry-transfected nuclei were captured at an excitation wavelength of 587 nm, emission wavelength of 610 nm, a light source intensity of 2% and an exposure time of 80 ms.

Data analysis of spheroid protrusion creep
The creep length $L(t)$ of the spheroid protrusion edges over time was extracted from the experimental images using Fiji (https://imagej.net/software/fiji/) and a custom-written Python script (which is available at: https://github.com/RubenBoot/HighThroughput_Spheroid_MPA/blob/main/SpheroidAspiration_AnalysisScript.py) previously introduced and explained in Ref.[25]. In short, the brightfield time-lapse images are cropped to the region of interest and binarized (using the Thresholding function from Fiji) to provide a clear contrast between the protrusion edge and the surrounding channel. The script detects the distance from the protrusion edge to the start of the constriction channel and writes all results in a Microsoft Excel file alongside the time step per image. If the protrusion edge did not maintain its integrity due to cells breaking off, or if spheroids did not retain a constant volume and roundness during aspiration, they were omitted from the analysis.

The viscous creep rates L_∞^a and L_∞^r and the elastic deformation length δ_a were derived by fitting a modified Maxwell model to the creep curve $L(t)$ [for full derivation see Supplementary Information]. Further mechanical parameters, such as the critical pressure ΔP_c, surface tension γ and viscosity η were derived from these fitted parameters as explained in the Supplementary Information.

Statistical analysis
Statistical comparisons between two distributions were done with a two-sided t-test. These were executed using the TTEST function in Microsoft Excel. Fitting lines to data was executed using the Regression function in Microsoft Excel. We quote the p-value for these line fits as significance values to rejections of the null hypothesis. For both the two-sided t-tests and the line fits, we use the symbols *, ** and *** for $p < 0.05$, 0.01 and 0.001 respectively. The average human error in reading off the aspiration pressure when manually lowering the outlet vial is $0.2\,cmH_2O$ (~ 20 Pa), defined by the thickness of the lines on the ruler indicating the distances. The error in dimensions of the aspiration channel was measured with a Dektak Stylus Profiler (Bruker) and determined

to be 5 μm. Error bars in the figures display the standard error of the mean unless indicated otherwise, and are always based on at least three independent days of experiments.

Data availibility

References

1. Hahn, C. & Schwartz, M. A. Mechanotransduction in vascular physiology and atherogenesis. *Nat. Rev. Mol. Cell Biol.* **10**, 53–62. https://doi.org/10.1038/nrm2596 (2009).
2. Mammoto, T. & Ingber, D. E. Mechanical control of tissue and organ development. *Development* **137**, 1407–1420. https://doi.org/10.1242/dev.024166 (2010).
3. Brugués, A. *et al.* Forces driving epithelial wound healing. *Nat. Phys.* **10**, 683–690. https://doi.org/10.1038/nphys3040.Forces (2014).
4. Discher, D. E., Mooney, D. J. & Zandstra, P. W. Growth factors, matrices, and forces combine and control stem cells. *Science* **324**, 1673–1677. https://doi.org/10.1126/science.1171643 (2009).
5. Nia, H. T. *et al.* Solid stress and elastic energy as measures of tumour mechanopathology. *Nat. Biomed. Eng.* **1**, 1–25. https://doi.org/10.1038/s41551-016-0004.Solid (2016).
6. Nia, H. T., Munn, L. L. & Jain, R. K. Physical traits of cancer. *Science*. **370**, eaaz0868. https://doi.org/10.1126/SCIENCE.AAZ0868 (2020).
7. Galie, P. A., Georges, P. C. & Janmey, P. A. How do cells stiffen?. *Biochem. J.* **479**, 1825–1842. https://doi.org/10.1042/BCJ20210806 (2022).
8. Friedl, P., Wolf, K. & Lammerding, J. Nuclear mechanics during cell migration. *Curr. Opin. Cell Biol.* **23**, 55–64. https://doi.org/10.1016/j.ceb.2010.10.015 (2011).
9. Schiele, N. R. *et al.* Actin cytoskeleton contributes to the elastic modulus of embryonic tendon during early development. *J. Orthop. Res.* **33**, 874–881. https://doi.org/10.1002/jor.22880 (2015).
10. Heisenberg, C. P. & Bellaïche, Y. Forces in tissue morphogenesis and patterning. *Cell* **153**, 948–962. https://doi.org/10.1016/j.cell.2013.05.008 (2013).
11. Han, Y. L. *et al.* Cell swelling, softening and invasion in a three-dimensional breast cancer model. *Nat. Phys.* **16**, 101–108. https://doi.org/10.1038/s41567-019-0680-8 (2020).
12. Jakab, K. *et al.* Relating cell and tissue mechanics: Implications and applications. *Develop. Dynam.* **237**, 2438–2449. https://doi.org/10.1002/dvdy.21684 (2008).
13. Kosheleva, N. V. *et al.* Cell spheroid fusion: Beyond liquid drops model. *Sci. Rep.* **10**, 1–15. https://doi.org/10.1038/s41598-020-69540-8 (2020).
14. Grosser, S. *et al.* Cell and nucleus shape as an indicator of tissue fluidity in carcinoma. *Phys. Rev. X* **11**, 011033. https://doi.org/10.1103/PhysRevX.11.011033 (2021).
15. Gonzalez-Rodriguez, D., Guevorkian, K., Douezan, S. & Brochard-Wyart, F. Soft matter models of developing. *Science* **82**, 910–917 (2012).
16. Boot, R. C., Koenderink, G. H. & Boukany, P. E. Spheroid mechanics and implications for cell invasion. *Adv. Phys. X* **6**, 1978316. https://doi.org/10.1080/23746149.2021.1978316 (2021).
17. Foty, R. A., Pfleger, C. M., Forgacs, G. & Steinberg, M. S. Surface tensions of embryonic tissues predict their mutual envelopment behavior. *Development* **122**, 1611–1620 (1996).
18. Ryan, P. L., Foty, R. A., Kohn, J. & Steinberg, M. S. Tissue spreading on implantable substrates is a competitive outcome of cell-cell vs. cell-substratum adhesivity. *Proc. Natl. Acad. Sci. USA* **98**, 4323–4327. https://doi.org/10.1073/pnas.071615398 (2001).
19. Schötz, E. M. *et al.* Quantitative differences in tissue surface tension influence zebrafish germ layer positioning. *HFSP J.* **2**, 42–56. https://doi.org/10.2976/1.2834817 (2008).
20. Foty, R. A. & Steinberg, M. S. The differential adhesion hypothesis: A direct evaluation. *Develop. Biol.* **278**, 255–263. https://doi.org/10.1016/j.ydbio.2004.11.012 (2005).
21. Brodland, G. W. The Differential Interfacial Tension Hypothesis (DITH): A comprehensive theory for the self-rearrangement of embryonic cells and tissues. *J. Biomech. Eng.* **124**, 188–197. https://doi.org/10.1115/1.1449491 (2002).
22. Manning, M. L., Foty, R. A., Steinberg, M. S. & Schoetz, E. M. Coaction of intercellular adhesion and cortical tension specifies tissue surface tension. *Proc. Natl. Acad. Sci. USA* **107**, 12517–12522. https://doi.org/10.1073/pnas.1003743107 (2010).
23. Guevorkian, K., Colbert, M.-J., Durth, M., Dufour, S. & Brochard-Wyart, F. Aspiration of biological viscoelastic drops. *Phys. Rev. Lett.* **104**, 1–4. https://doi.org/10.1103/PhysRevLett.104.218101 (2010).
24. Yousafzai, M. S. *et al.* Active regulation of pressure and volume defines an energetic constraint on the size of cell aggregates. *Phys. Rev. Lett.* **128**, 48103. https://doi.org/10.1103/physrevlett.128.048103 (2022).
25. Boot, R. C. *et al.* High-throughput mechanophenotyping of multicellular spheroids using a microfluidic micropipette aspiration chip. *Lab Chip* **23**, 1768–1778. https://doi.org/10.1039/d2lc01060g (2023).
26. Davidson, P. M. *et al.* High-throughput microfluidic micropipette aspiration device to probe time-scale dependent nuclear mechanics in intact cells. *Lab Chip* **19**, 3652–3663. https://doi.org/10.1039/c9lc00444k (2019).
27. Son, Y. Determination of shear viscosity and shear rate from pressure drop and flow rate relationship in a rectangular channel. *Polymer* **48**, 632–637. https://doi.org/10.1016/j.polymer.2006.11.048 (2007).
28. Guevorkian, K., Brochard-Wyart, F. & Gonzalez-Rodriguez, D. *Flow Dynamics of 3D Multicellular Systems into Capillaries* (Academic Press, 2021).
29. Guevorkian, K., Gonzalez-rodriguez, D., Carlier, C., Dufour, S. & Brochard-Wyart, F. Mechanosensitive shivering of model tissues under controlled aspiration. *PNAS* **108**, 13387–13392. https://doi.org/10.1073/pnas.1105741108 (2011).
30. Scanlon, C. S., Van Tubergen, E. A., Inglehart, R. C. & D'Silva, N. J. Biomarkers of epithelial-mesenchymal transition in squamous cell carcinoma. *J. Dental Res.* **92**, 114–121. https://doi.org/10.1177/0022034512467352 (2013).
31. Hinz, B., Celetta, G., Tomasek, J. J., Gabbiani, G. & Chaponnier, C. Alpha-smooth muscle actin expression upregulates fibroblast contractile activity. *Mol. Biol. Cell* **12**, 2730–2741. https://doi.org/10.1091/mbc.12.9.2730 (2001).
32. Sarrió, D. *et al.* Epithelial-mesenchymal transition in breast cancer relates to the basal-like phenotype. *Cancer Res.* **68**, 989–997. https://doi.org/10.1158/0008-5472.CAN-07-2017 (2008).
33. Doolin, M. T., Smith, I. M. & Stroka, K. M. Fibroblast to myofibroblast transition is enhanced by increased cell density. *Mol. Biol. Cell* **32**, 1–9. https://doi.org/10.1091/mbc.E20-08-0536 (2021).
34. Yu, M. *et al.* Coherent timescales and mechanical structure of multicellular aggregates. *Biophys. J.* **114**, 2703–2716. https://doi.org/10.1016/j.bpj.2018.04.025 (2018).

35. Janmey, P. A. & Weitz, D. A. Dealing with mechanics: Mechanisms of force transduction in cells. *Trends Biochem. Sci.* **29**, 364–370. https://doi.org/10.1016/j.tibs.2004.05.003 (2004).
36. Martino, F., Perestrelo, A. R., Vinarský, V., Pagliari, S. & Forte, G. Cellular mechanotransduction: From tension to function. *Front. Physiol.* **9**, 1–21. https://doi.org/10.3389/fphys.2018.00824 (2018).
37. Sbrana, F. *et al.* Role for stress fiber contraction in surface tension development and stretch-activated channel regulation in C2C12 myoblasts. *Am. J. Physiol. Cell Physiol.* **295**, 160–172. https://doi.org/10.1152/ajpcell.00014.2008 (2008).
38. Delanoe-Ayari, H., Kurdi, R. A., Vallade, M., Gulino-Debrac, D. & Riveline, D. Membrane and acto-myosin tension promote clustering of adhesion proteins. *PNAS* **101**, 2229–2234. https://doi.org/10.1073/pnas.0304297101 (2004).
39. Ingber, D. E. Cellular mechanotransduction: Putting all the pieces together again. *FASEB J.* **20**, 811–827. https://doi.org/10.1096/fj.05-5424rev (2006).
40. Kaunas, R. & Deguchi, S. Multiple roles for Myosin II in tensional homeostasis under mechanical loading. *Cell. Mol. Bioeng.* **4**, 182–191. https://doi.org/10.1007/s12195-011-0175-x (2011).
41. Foty, R. A. & Steinberg, M. S. Cadherin-mediated cell-cell adhesion and tissue segregation in relation to malignancy. *Int. J. Dev. Biol.* **48**, 397–409 (2004).
42. Pawlizak, S. *et al.* Testing the differential adhesion hypothesis across the epithelial-mesenchymal transition. *N. J. Phys.* **17**, 083049. https://doi.org/10.1088/1367-2630/17/8/083049 (2015).
43. Marmottant, P. *et al.* The role of fluctuations and stress on the effective viscosity of cell aggregates. *PNAS* **106**, 17271–17275. https://doi.org/10.1073/pnas.0902085106 (2009).
44. David, R. *et al.* Tissue cohesion and the mechanics of cell rearrangement. *Development* **141**, 3672–3682. https://doi.org/10.1242/dev.104315 (2014).

Acknowledgements

Author contributions

R.C.B., A.N., C.G., D.H.M., G.H.K. and P.E.B. conceived the experiments; R.C.B., A.N., C.G. and P.M. conducted the experiments; R.C.B. and A.N. analysed the results. R.C.B. wrote the manuscript. All authors reviewed the manuscript.

Competing interests

The authors declare no competing interests.

Additional information

Supplementary Information The online version contains supplementary material available at https://doi.org/10.1038/s41598-024-70759-y.

Correspondence and requests for materials should be addressed to P.E.B.

Reprints and permissions information is available at www.nature.com/reprints.

Publisher's note Springer Nature remains neutral with regard to jurisdictional claims in published maps and institutional affiliations.